High Kinetic Inductance in Platinum-Coated Aluminum Nanobridge Interferometers

Ivan A Nazhestkin, Sergey V Bakurskiy, Alex A Neilo, Irina E Tarasova, Nidzhat G Ismailov, Vladimir L Gurtovoi, Sergey V Egorov, Sergey A Lisitsyn, Vasily S Stolyarov, Vladimir N Antonov, et al.

High Kinetic Inductance in Platinum-Coated Aluminum Nanobridge Interferometers

Ivan A. Nazhestkin, Sergey V. Bakurskiy, Alex A. Neilo, Irina E. Tarasova, Nidzhat G. Ismailov, Vladimir L. Gurtovoi, Sergey V. Egorov, Sergey A. Lisitsyn, Vasily S. Stolyarov, Vladimir N. Antonov, Valery V. Ryazanov, Mikhail Y. Kupriyanov, Igor I. Soloviev, Nikolay V. Klenov, and Dmitry S. Yakovlev*

The transport properties of a nanobridge superconducting quantum interference device made of Al/Pt bilayer have been studied. Measurement and approximation of the voltage-field dependencies allow to estimate the inductance of the structure. It is found that this value significantly exceeds the expected geometric inductance and exhibits an atypical temperature dependence. To explain this effect, a microscopic model of electron transport in SN bilayers is developed, considering the proximity effect, and the available regimes of the current distribution are described. The measured properties may be indicative of the formation of high-resistance aluminum with high values of kinetic inductance during the fabrication of Al/Pt bilayers.

1. Introduction

Thin-film aluminum structures have long been the foundation of superconducting quantum technologies.[1–3] Over the past two decades, superconducting aluminum (Al) qubits demonstrated remarkable advancements in the coherence times and gate fidelity, thus becoming a leading technology for quantum computing.[4,5] However, defects and impurities at the interfaces and surfaces remain a significant hurdle in achieving scalable quantum systems.[6–8] It is established that the surface oxide that spontaneously forms on aluminum under ambient conditions is a

primary source of microwave loss and decoherence.[8–10] Coating aluminum with protective layers, such as noble metals, has shown a significant reduction in the effect.[11–13] However, the bilayers of a superconductor (S) and a normal (nonsuperconducting, N) metal have several properties that require further attention. One of them is the relatively high kinetic inductance of S/N bilayers, which may work in positive and negative directions.

Kinetic inductance (KI) refers to the inductance of a film due to the inertia of its carriers. The concentration of quasiparticles becomes exponentially small below the critical temperature $T \ll T_c$ (typical of modern quantum technologies), and the surface impedance of the superconductor is primarily governed by the KI, which arises from the kinetic energy of the Cooper pairs. Superconducting films exhibiting high KI have been used in microwave kinetic inductance detectors (MKIDs),[14–18] superconducting single-photon detectors (SSPDs),[19–24] bolometers,[25–28] vortices detection,[29–32] parametric amplifiers (PAs),[33–38] rapid single-flux quantum (RSFQ) and neuromorphic circuits,[39–44] and more recently, superconducting qubit circuits (QCs).[3,45–50] Superconducting quantum interference devices (SQUIDs) made of such films have

I. A. Nazhestkin, I. E. Tarasova, V. L. Gurtovoi, S. V. Egorov, S. A. Lisitsyn, V. V. Ryazanov
Superconducting Quantum Computing Lab
Quantum Center
Skolkovo, 143025 Moscow Region, Russia

I. A. Nazhestkin, I. E. Tarasova, V. S. Stolyarov, V. V. Ryazanov
Moscow Institute of Physics and Technology
141700 Dolgoprudny, Russia

S. V. Bakurskiy, A. A. Neilo, M. Y. Kupriyanov, I. I. Soloviev
Skobeltsyn Institute of Nuclear Physics
Moscow State University
Leninskie gory, GSP-1, 119991 Moscow, Russia

N. G. Ismailov, N. V. Klenov
Faculty of Physics
Moscow State University
119991 Moscow, Russia

V. N. Antonov
Skolkovo Institute of Science and Technology
Bolshoy boul., 30, 121205 Moscow, Russia

D. S. Yakovlev
Laboratoire de Physique et d'Etude des Matériaux
ESPCI Paris
PSL Research University
CNRS
Sorbonne University
75005 Paris, France
E-mail: dimitry.yakovlev@espci.fr

**ADVANCED
SCIENCE NEWS**

www.advancedsciencenews.com

**ADVANCED
ENGINEERING
MATERIALS**

www.aem-journal.com

shown flux sensitivities as high as the single electron spin-flip detection. The devices have been fabricated using various pure superconducting materials such as Al, grAl, Nb, NbN, TiN, or MoRe,[51–59] as well as the bilayer superconductor/normal metal films.

In this work, we conduct an experimental and theoretical study of the kinetic inductance of platinum-coated aluminum films. The bilayer is used to fabricate SQUID with the Dayem nanobridges instead of the traditional Josephson junctions (JJs). In such a design, the Pt layer acts as a thermal shunt, providing effective thermalization of the system. This effect in Al/Pt nanobridges suppresses the hysteresis of the I–V curve,[60] a common problem of SQUIDs. As a result, we can carry out experiments in a wide cryogenic temperature range, down to 10 mK. We have found an interesting property of the Al/Pt bilayer: a high kinetic inductance, which is several orders of magnitude larger than the geometric inductance over a wide temperature range.

By analyzing experimental data, we arrived at a consistent microscopic theory of the observed effect. The study sheds light on the phenomenon of the kinetic inductance in hybrid S/N bilayers and opens avenues for their wider application to quantum technologies, such as tunable inductive elements in quantum circuits and noise-resistant detectors.

2. Experimental Section

The schematic of the SQUID with Dayem bridges is depicted in **Figure** 1a. It consists of a superconducting ring with four interconnecting terminals and nanobridges. The SQUID is made of a 27/10 nm-thick Al/Pt film. Technology of device fabrication is given in detail in our previous study.[60] Terminals $V+$ and $V-$ are utilized to measure the switching voltage, while terminals $I+$ and $I-$ are designated for the bias current. Figure 1b shows a scanning electron microscopy (SEM) image of the device. The SQUID has 2 µm diameter loop. The nanobridges 32 nm wide, as shown in Figure 1c, are significantly smaller than the thin-film penetration depth $\lambda_{\text{thin}} = \lambda^2/d$, where d represents the thickness of the film, and λ is the bulk penetration depth.[61]

Energy-dispersive X-ray spectroscopy (EDXS) colormap bilayer Al/Pt intermetallic structure is shown in Figure 1d. EDXS chemical distribution maps are obtained from spectral intensities of the aluminum (light green), platinum (blue), silicon (yellow), and oxygen (red), respectively. The cross-sectional morphology and EDXS analysis confirmed the formation of the bilayer is formed without oxide between the Al and Pt.

The transport measurements of the sample are done by standard four-point technique in ^{3}He–^{4}He dilution refrigerator in the temperature range from 15 mK to 15 K. The measurements are performed with a room-temperature differential amplifier. Current bias is applied symmetrically through accurately matched precise resistors. To improve the accuracy of the current bias, an inverted voltage drop on the sample is used as a reference for the differential amplifier. The power lines of the amplifier are filtered with 1 µF capacitors to decouple the amplifier

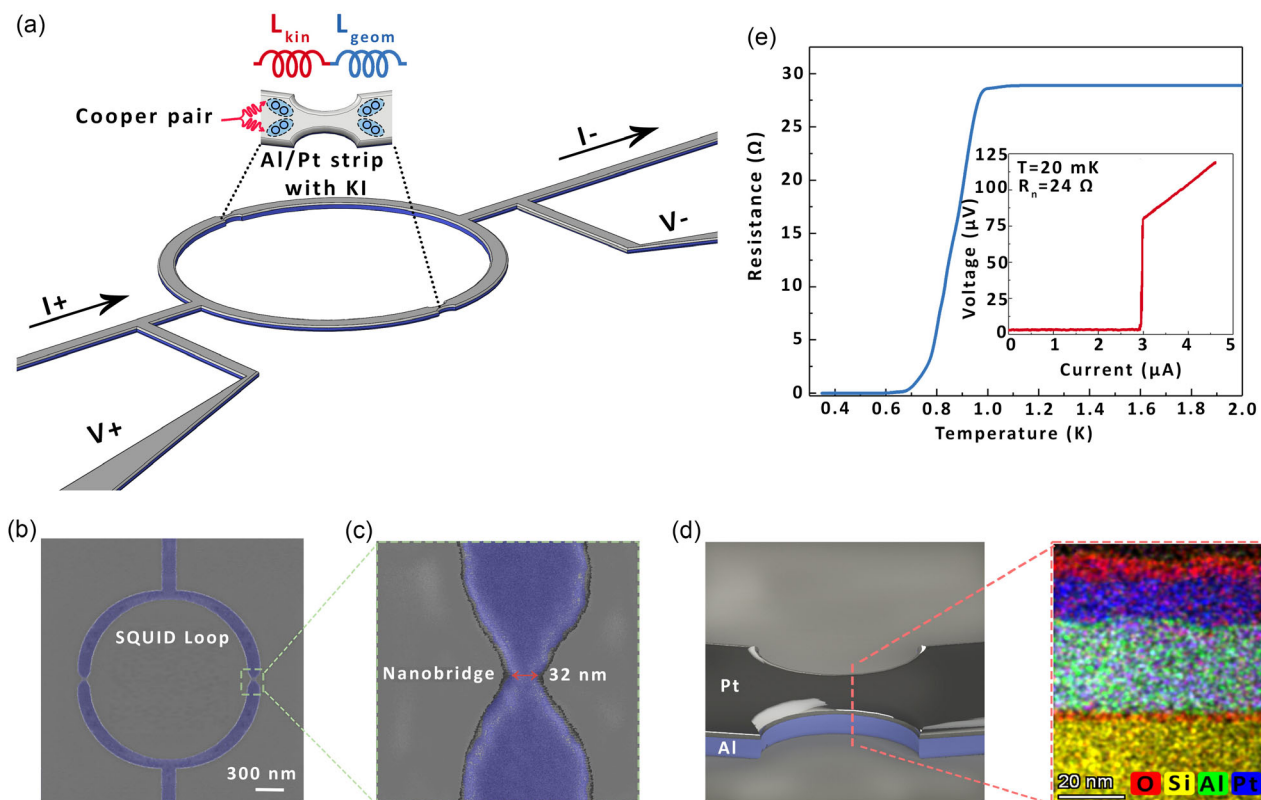**Figure 1.** a) Schematic circuit of an Al/Pt bilayer nanobridge SQUID. A nanobridge section of SQUID is zoomed in at the top. b) SEM image of the device. c) Zoomed image of one of the nanobridges. It is 32 nm wide at the narrowest point. d) EDX map image of the layered nanobridges. e) Temperature dependence of the SQUID resistance at 10 nA current bias; the insert shows typical I–V curve at the base temperature $T = 20$ mK.

**ADVANCED
SCIENCE NEWS**

www.advancedsciencenews.com

**ADVANCED
ENGINEERING
MATERIALS**

www.aem-journal.com

schematic from 50 Hz harmonics. The measurement scheme details are described elsewhere.[62,63]

Figure 1e shows the $R(T)$ curve of the measured sample. There is a superconducting transition of Al/Pt film at ≈ 1 K. Due to the proximity effect,[64,65] the critical temperature is lower than that of the pure Al film produced under the same technological conditions,[60] which is around 1.4 K. The critical current and normal-state resistance of nanobridges at 20 mK are $I_c = 3\ \mu A$ and $R_n \approx 24\ \Omega$.

We measure the voltage-field curves of the SQUID at different bias currents; see **Figure 2**a. One can see a modulation of the voltage with a period corresponding to the superconducting flux quantum through the area of the SQUID loop. The amplitude of the modulation decreases with increasing bias current. From the above data, it appears that the real inductance of the circuit is several orders of magnitude larger than the value obtained from direct estimates of its geometric inductance ($L_{loop} = \mu_0 \cdot 2r \approx 2.72$ pH). Let's look at the possible causes of this oddity in the next section.

3. Theoretical Methods and Results

3.1. Distribution of the Current Density in SQUIDs

To explain the discrepancy between the predicted inductance and experimental value, we calculate the current density distribution in the SQUID using the 3D-MLSI software.[66] The results are shown in Figure 2d. The model is based on solving the London and Maxwell equations on the triangular mesh using the finite element method. The equations are solved under the approximations that the current flows in the 2D surface, which is correct in cases when $d \ll 1$ and $d \approx \lambda_L$, where d is the film thickness, l is the characteristic structure size, and λ_L is the London penetration depth. Then, the algorithm of 3D-MLSI software package estimates the inductance of the SQUID in a few steps. Firstly, the distribution of the supercurrent density $j(\vec{r})$ and the flux function $\psi(\vec{r}) = \nabla j(\vec{r})$ are calculated. Then, the integral energy expression is derived and
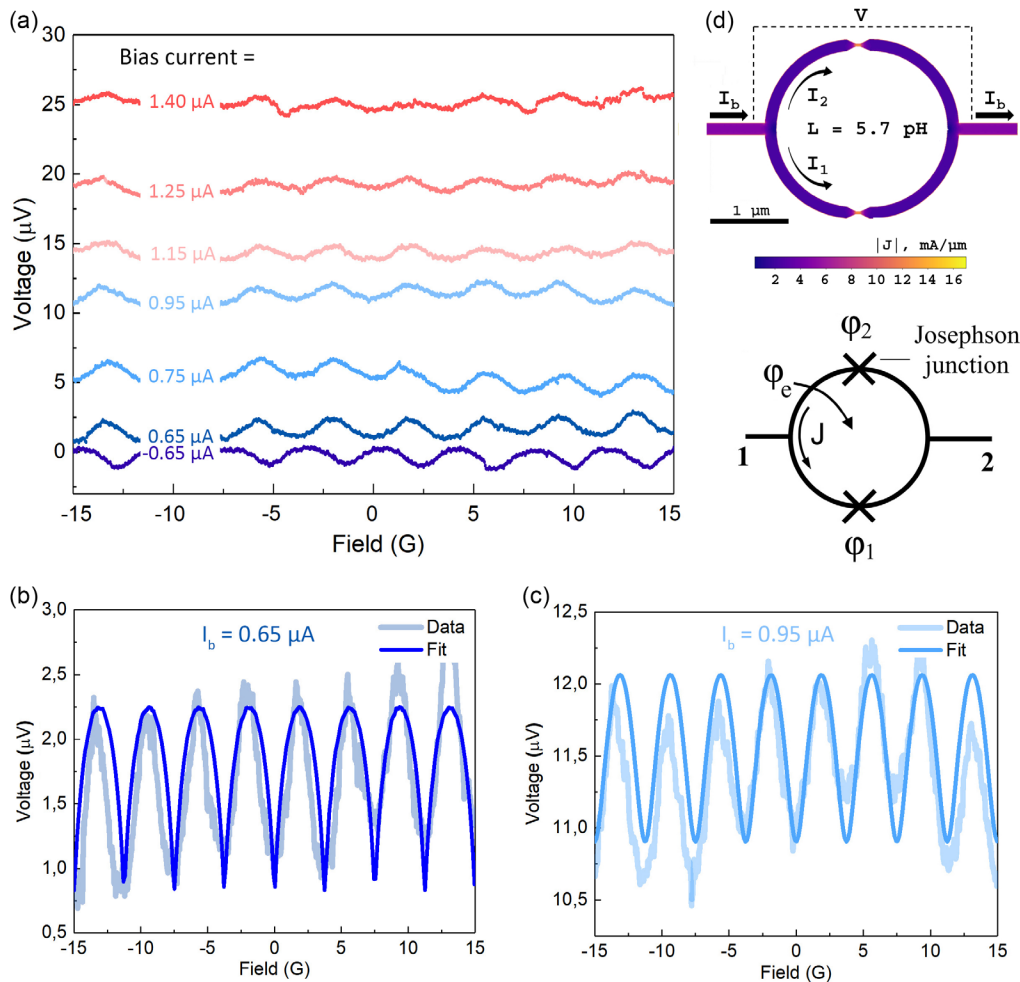
Figure 2. a) Voltage-field $V(B)$ curves for SQUID at different bias currents. The period of oscillations is ≈ 3.5 Gs. b) Modeling of voltage-field $V(B)$ curves with the resistively shunted junction (RSJ) model at bias currents $I_{bias} = 0.65\ \mu A$. c) $I_{bias} = 0.95\ \mu A$ (solid lines). d) 3D-MLSI simulation of the current distribution in a dc SQUID ($2 \times 2\ \mu m^2$ loop, $30 \times 30\ nm^2$ junction). The simulation shows the normalized density of the current flowing through the superconductor and the schematic circuit diagram of the SQUID. Below is an equivalent circuit with two well-localized regions where a phase jump of the superconducting order parameter occurs (φ_1 and φ_2). The applied magnetic field corresponds to a normalized flux ϕ_{ext}; $J = I_2 - I_1$.

minimized. The simulation gives the SQUID loop inductance of $L = 5.7$ pH.

The aluminum London penetration depth $\lambda_L = 50$ nm and the film thickness $d = 27$ nm are used in the calculation. The equations are solved on the $h = 3.91$ nm mesh, which is reduced to $h_b = 1.95$ nm near the SQUID boundaries. These sizes are much smaller than the London penetration depth and the minimum SQUID dimensions (30 nm for bridges). To ensure the stability and convergence of the solution, we varied the mesh sizes. We found the variance of the estimated kinetic inductance around 0.01 pH, which is $\approx 0.1\%$ of the estimated value. As we can see, the values for the SQUID inductance that are obtained still cannot explain the experimental results.

3.2. SQUID Inductance from the Experimental Curves

The SQUID inductance can be extracted from the voltage-field $V(B)$ curves by fitting with the well-known RSJ model (Figure 2b,c).[67,68] The current across each junction (Dayem bridge) is written as follows.

$$I_{JJ} = \frac{\hbar C_J}{2e}\frac{d^2\varphi}{dt^2} + \frac{\hbar}{2eR_J}\frac{d\varphi}{dt} + I_c \sin\varphi \tag{1}$$

where C_J is the capacitance of a junction, R_J is the resistance of a junction, I_c is the critical current, and φ is the wave function phase difference across the junction. The capacitance of Dayem bridges is small and can be neglected. According to Kirchoff's law, the given bias current is the sum of two currents across junctions

$$I_b = \frac{\hbar}{2eR_{J1}}\frac{d\varphi_1}{dt} + I_{c1}\sin\varphi_1 + \frac{\hbar}{2eR_{J2}}\frac{d\varphi_2}{dt} + I_{c2}\sin\varphi_2 \tag{2}$$

Here φ_1, φ_2 denote the phase differences on the banks of junctions 1 and 2; I_{c1}, I_{c2} refer to their critical currents; R_{J1}, R_{J2} are the resistances, shunting junctions 1 and 2 in the RSJ-model. Substituting $i_b = \frac{I_b}{I_{c1}}$ and $t = \frac{\tau}{\omega_c}$ (where $\omega_c = \frac{2e}{\hbar}I_{c1}R_{J1}$), one can make this equation dimensionless

$$\dot{\varphi}_1 = i_b - \sin\varphi_1 - \alpha\dot{\varphi}_2 - \eta\sin\varphi_2 \tag{3}$$

Here, the parameters $\eta = \frac{I_{c2}}{I_{c1}}$ and $\alpha = \frac{R_{J1}}{R_{J2}}$ are responsible for the asymmetry of inductance and resistance of SQUID weak links, correspondingly. From the other side, the total magnetic flux over the SQUID can be written as follows.

$$\Phi = \Phi_e - L_1 I_1 + L_2 I_2 \tag{4}$$

where Φ_e is the external magnetic flux and $L_{1,2}$ are the inductances of SQUID arms. Substituting currents over arms, one can write

$$\Phi = \Phi_e - L_1\left(\frac{\hbar}{2eR_{J1}}\frac{d\varphi_1}{dt} + I_{c1}\sin\varphi_1\right) + L_2\left(\frac{\hbar}{2eR_{J2}}\frac{d\varphi_2}{dt} + I_{c2}\sin\varphi_2\right) \tag{5}$$

Now, one can make a substitution $\beta_{L1} = \frac{L_1}{L_J}, \beta_{L2} = \frac{L_2}{L_J}$, where $L_J = \frac{\hbar}{2eI_{c1}}$ and also make this equation dimensionless

$$\varphi_1 - \varphi_2 = \varphi_e - \beta_{L1}(\dot{\varphi}_1 + \sin\varphi_1) + \beta_{L2}(\alpha\dot{\varphi}_2 + \eta\sin\varphi_2) \tag{6}$$

From (3) and (6), one can write a final equation system which can be used to describe $V(B)$ curves

$$\begin{cases} \dot{\varphi}_1 = \frac{L_2}{L_1+L_2}\left(i_b + (\varphi_1 - \varphi_2 - \varphi_e)\frac{1}{L_2}\right) - \sin\varphi_1 \\ \dot{\varphi}_2 = \frac{L_1}{\alpha(L_1+L_2)}\left(i_b + (\varphi_1 - \varphi_2 - \varphi_e)\frac{1}{L_1}\right) - \frac{\eta}{\alpha}\sin\varphi_2 \end{cases} \tag{7}$$

From that, voltage-flux characteristics can be derived as

$$\frac{V}{I_{c_1}R_{J1}} = \frac{L_2}{L_1+L_2}\dot{\varphi}_1 + \frac{L_1}{L_1+L_2}\dot{\varphi}_2 \tag{8}$$

We emphasize that this simple method allows us to trace the influence of the scattering of the parameters of the Josephson contacts in our experiment.

Nota bene: An asymmetry in the critical currents of the Josephson contacts in the SQUID can reduce the modulation depth of $V(B)$. However, the effect will only be noticeable if the difference is unrealistically large. In addition, such an asymmetry shifts the positions of the zero of the $V(B)$ curve, which is not seen in the experiment.

3.3. Model of Kinetic Inductance in Microscopic Theory

To calculate the kinetic inductance of the S/N bilayer, we numerically solved the boundary problem in the framework of self-consistent Usadel equations[69]

$$\pi k_B T_c \xi^2\left(G\frac{d^2F}{dx^2} - F\frac{d^2G_p}{dx^2}\right) - \omega F = -G\Delta, G_\omega^2 + F_\omega F_{-\omega}^* = 1 \tag{9}$$

$$\Delta\ln\frac{T}{T_c} + \pi k_B T\sum_{\omega=-\infty}^{\infty}\left(\frac{\Delta}{|\omega|} - F\right) = 0 \tag{10}$$

with Kupriyanov–Lukichev boundary conditions[70]

$$\gamma_B\xi_l\left(\frac{dF_l}{dx} - \frac{F_l}{G_l}\frac{dG_l}{dx}\right) = F_r - F_l\frac{G_r}{G_l} \tag{11}$$

Here, G is the normal Green function, F is the anomalous Green function corresponding to the pair amplitude, Δ is the pair potential, and $\omega = \pi T(2n+1)$ are the Matsubara frequencies, where n is an integer. The nonlinear problem is solved iteratively with loops on $G(x)$ and $\Delta(x)$.

The calculated spatial distribution of the pairing amplitude allows estimation of the penetration depth distribution

**ADVANCED
SCIENCE NEWS**

www.advancedsciencenews.com

**ADVANCED
ENGINEERING
MATERIALS**

www.aem-journal.com

$$\lambda^{-2}(x) = \lambda_0^{-2}\frac{T}{T_c}\frac{\rho_S}{\rho}\sum_{\omega>0}\mathrm{Re}(F(x)^2); \quad \lambda_0^{-2} = \frac{2\pi\mu_0 k_B T_c}{\rho_S \hbar} \quad (12)$$

and corresponding kinetic inductance of the S/N bilayer

$$L_K = \frac{\mu_0 X}{W}\left[\int_0^d (\lambda(x))^{-2}\mathrm{d}x\right]^{-1} \quad (13)$$

The spatial distribution of the order parameter and thus the properties of the kinetic inductance in the S/N bilayer depend strongly on the parameters and thicknesses of the film.[71–75] In the proximity effect, the ratio of the layer thicknesses d_s and d_n and the coherence lengths ξ_s and ξ_n play an important role. The key parameters of the modeling are the boundary resistivity $\gamma_B = \frac{R}{\rho_n\xi_n}$, which depends on the specific resistivity of the boundary R, and $\gamma = \frac{\rho_s\xi_s}{\rho_n\xi_n}$, determined by the spatial area in which the order parameter is suppressed due to the proximity effect. The general types of the spatial distribution of pair amplitude F (left column) and inverse square of penetration depth λ^{-2} (right column) are shown in **Figure 3**. Note that the spatial distribution of the current $j(x)$ is proportional to λ^{-2} and can also be estimated from the right column of Figure 3.

In the case of $\gamma \gg 1$, superconductivity suppression occurs principally in the region of the superconductor, leading to a significant decrease in the critical temperature and weak penetration of superconducting correlations into the normal metal layer (Figure 3c,d). In the opposite case, $\gamma \ll 1$, the pairing amplitude decreases in the normal metal region. In this case, the suppression of the critical temperature is weak, and the normal layer has nonzero pairing amplitude (Figure 3a,b). An increase in the specific resistance at the boundary (and hence the parameter γ_B) leads to a weakening of the proximity effect, which is accompanied by a decrease in both the suppression of the critical temperature and the penetration of paired correlations into the normal layer.

The distribution of currents in the bilayers is determined by the ratio of the inductance of the layers, L_K in (13). The reverse inductance is proportional to the square of the pairing amplitude, which is fully determined by the proximity effect calculation and is inversely proportional to the resistivity of the layer. Such dependence provides the special case for low-resistance metal with high coherence length $\gamma \leq 1$ and $\rho_n \ll \rho_s$ (Figure 3i,j). In this case, a sufficiently high pairing amplitude of the low-resistance metal makes the effective kinetic inductance of the normal layer lower than that of the superconducting layer. Then, the supercurrent flows mainly through the normal metal.

This is the operating limit[76] for many S/N structures, which are actively used to make single-photon detectors[77,78] and nonlinear elements for parametric amplifiers.[79] They work in the following way: when the current concentration increases, the superconductivity in the normal metal layer is destroyed, leading to current flow into the superconducting layer and a significant change in the kinetic inductance.

In the alternative limit of high-resistive (compared to a superconductor) normal metal, the current flows through the superconducting layer. In this case, the main effect of normal metal on top of a superconductor is a decrease in the critical
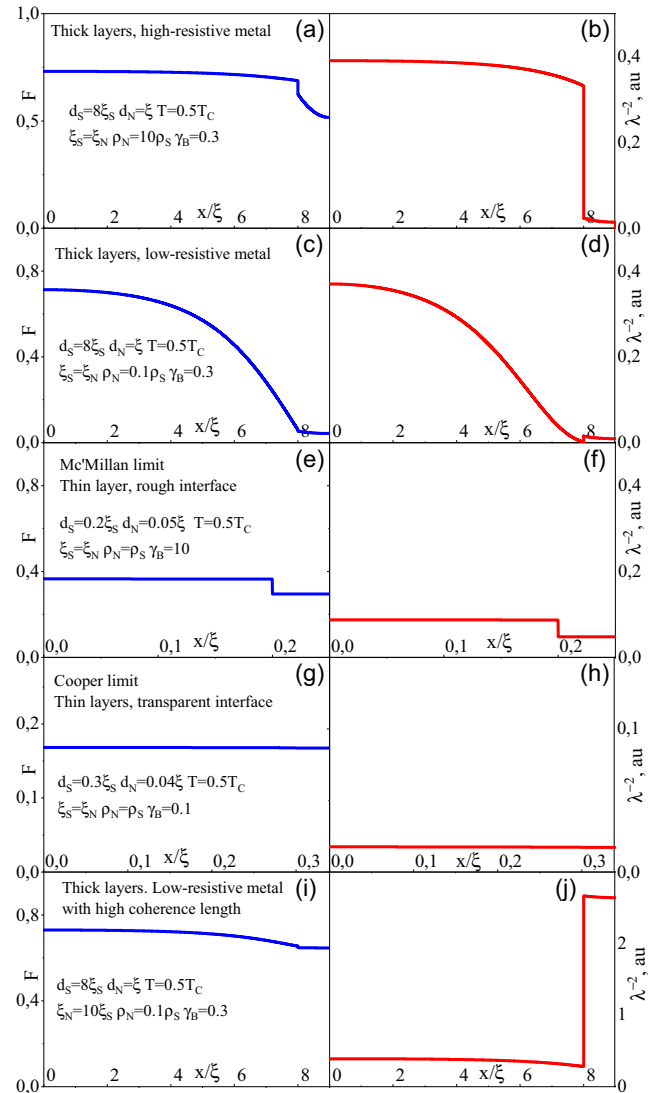

Figure 3. Spatial distribution of pair amplitude $F(x)$ (left column) and inverse square penetration depth λ^2 (right column) for common types of S/N bilayers as a function of layer thickness, material parameters, and interface quality. a,b) Parameter $\gamma = \frac{\rho_s\xi_s}{\rho_n\xi_n} \gg 1$, the pairing amplitude decreases in the normal metal region, the suppression of the critical temperature is weak, and the normal layer has nonzero pairing amplitude. c,d) $\gamma \gg 1$, superconductivity suppression occurs principally in the region of the superconductor, leading to a significant decrease in the critical temperature and weak penetration of superconducting correlations into the normal metal layer. e,f) McMillan (thin layers with opaque boundary) limit: $d_s \ll \xi_s$, $d_n \ll \xi_n$, $\gamma_B \gg 1$. g,h) Cooper limit ($d_s \ll \xi_s$, $d_n \ll \xi_n$, $\gamma_B \ll 1$). i,j) Low-resistance metal with high coherence length $\gamma \leq 1$ and $\rho_n \ll \rho_s$, high pairing amplitude of the low-resistance metal makes the effective kinetic inductance of the normal layer lower than that of the superconducting layer. Then, the supercurrent flows mainly through the normal metal.

temperature and suppression of the superconductivity. The pair of crystalline Al ($\xi_{Al} = 120$ nm, $\rho_{Al} = 1.8\,\mu\Omega$ cm)[80] and Pt ($\xi_{Pt} = 32$ nm, $\rho_{Pt} = 11\,\mu\Omega$ cm)[81] presumably makes this limit. Depending on the resistivity parameter of the boundary γ_B, the critical temperature can be shifted significantly. As a result,

the kinetic inductance of the bilayer film in the operating temperature range can be several times higher than its value at low temperatures. Because of the shift of the critical temperature, hybrid structures based on aluminum layers are actively used for kinetic inductance detectors.[82–84]

In the limit of thin layers, $d_s \ll \xi_s$ and $d_n \ll \xi_n$, the solution of the Usadel equation has specifics. The spatial distribution of the pairing amplitude in each layer becomes constant. For the transparent boundary, $\gamma_B \ll 1$, the Cooper limit[85] is realized, where the superconductivity in the layers is averaged, and the bilayer can be considered as a single superconductor with suppressed T_c (Figure 3g,h). For an opaque boundary, $\gamma_B \gg 1$, the McMillan[86] limit is realized: the normal layer is weakly proximized (Figure 3e,f), and the critical temperature can be estimated as

$$T_C^* = T_C\left(1 - \frac{\pi^2 \xi_s}{2\gamma_B d_s}\right) \quad (14)$$

4. Discussion

We estimate the kinetic inductance of the Al/Pt bilayer using Equation (10)–(13) and compare it with the experiment; see Figure 2b,c. Each arm of the SQUID is a sequential connection of a nanobridge of 50 nm long and 32 nm wide, and a half-ring of 2 μm diameter and 150 nm wide. Josephson effect in such a SQUID is associated with the phase slip in nanobridges. At the same time, the inductance of the arm is determined by the half-ring. It exceeds the inductance of nanobridge by a factor of more than 10. We calculate the geometric part of inductance using the 3D-MLSI simulation software package.[87–89] Using the sample parameters from **Table 1**, we find geometrical inductance of 5.7 pH. At the same time, the estimation of the inductance of the SQUID arm from the experimental voltage-field dependencies $V(B)$ gives us 5–10 nH in the temperature range from 0.3 up to 0.7 K, and this value increases with increasing temperature (see the red dots in **Figure 4**a,b). Thus, the estimated geometrical inductance is three orders of magnitude lower than the value obtained from the experiment.

The calculation of the kinetic inductance of the diffusive bilayer of polycrystalline Al ($\rho = 1.8$ μΩ cm) and Pt ($\rho = 11$ μΩ cm) films is shown in Figure 4a. The value of the kinetic inductance at low temperatures is of the order of 100 pH. Near the critical temperature $T \approx 0.7$ K, the kinetic inductance can increase by orders of magnitude due to suppression of superconductivity. However, the inductance is almost equal to its low-temperature value in the wide range of lower temperatures. This shape of the $L_k(T)$ dependence contradicts the experimental data, which are represented by the red dots in Figure 4a.

Such discrepancy can be resolved by assuming a significant change in the morphology of aluminum upon platinum coating. Ref. [60] demonstrates that the sputtering of the Pt film above the Al layer increases the total resistance of the structure despite the
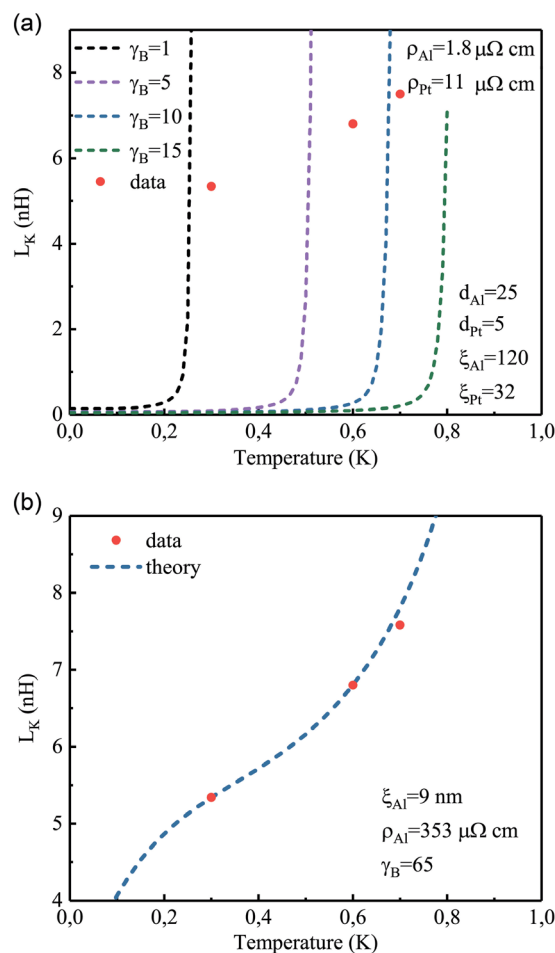

Figure 4. Inductance of the SQUID arm L_K made of 27/10 Al/Pt bilayer versus temperature T, calculated in the framework of the microscopic model for a) low resistivity crystal Al with $\rho = 1.8$ μΩ cm for different interface parameters γ_B and for b) high resistivity granulated Al with $\rho = 353$ μΩ cm. The red dots on panels (a,b) are the inductance taken from the fit of the field $V(B)$ dependence at different temperatures.

increase in the cross-sectional area of the strip. The increase in aluminum's resistivity may be explained by the formation of the intermetallic compounds Al/Pt.[90] The EDX map in Figure 1d partially confirms this assumption: on this map, one can see the inclusion of Pt clusters in the Al matrix.

Assuming the change of the Al-layer morphology, we solved the Usadel problem with free parameters ρ_{Al} and ξ_{Al} and tried to fit the experimental $L_K(T)$ data. We found that in the limit of the huge resistance $\rho_{Al} = 353$ μΩ cm and small coherence length $\xi_{Al} = 9$ nm, kinetic inductance is in the order of a few nH in the whole temperature range with monotonous growth with an increase of temperature; see Figure 4b.

Table 1. Relevant parameters for the measured device at 700 mK.

Sample	I_c [μA]	R_n^{exp} [Ω]	$W^{constriction}$ [nm]	d_A [nm]	d_{Pt} [nm]	L [nm]	δH [G]	A_{eff} [μm²]	T_c [K]	ρ_n [Ω nm]
Al/Pt	2.93	24	31 ± 1	27 ± 1	10 ± 1	50 ± 10	5.3	3.8	0.8	40.93

This transport regime significantly differs from that on which we based our preliminary estimates. Our numerical calculations show that despite the rather large magnitudes of $\gamma = 9$ and $\gamma_B = 65$, the small value of Pt thickness $d_N/\xi_N \approx 0.3$ allows the diffusion of the superconducting correlation from Al to Pt. Their magnitudes are weak, leading to a large difference between the energy gap in the density of state in Pt compared to that in Al. At the same time, the significant difference in resitivities $(\rho_s/\rho_N \approx 30$ leads to the concentration of a bias supercurrent in the N part of the SN bilayer. As a result, the kinetic inductance of Al/Pt bilayer depends on the temperature-sensitive weak proximization of Pt layer, providing atypical almost linear $L_K(T)$ dependence.

Calculated properties of the Al-layer from our fit are similar to granular aluminum, grAl. Granular aluminum has a resistivity in the range $\rho_{grAl} = 10 \dots 10^4\,\mu\Omega\,cm$ and a grain size of about 3 nm.[3,91–95] We guess that bilayers of grAl with low-resistive normal metals or crystalline Al should demonstrate the similar transport properties demonstrated in Figure 4b with high and growing kinetic inductance in the whole temperature range.

The assumption of high resistive aluminum allows us to explain the unexpectedly large kinetic inductance of the measured structure. However, the comparison of this model with the resistive transport measurements (Figure 1d) is an issue. The resistivity of the structure in the normal state is 24 Ω, which is inconsistent with estimates for both the low and high aluminum resistivity limits.

Rough estimates show that the resistance of the constriction is about 5–10 times smaller than the resistance of the SQUID arm. In the case of a crystalline aluminum structure with $\rho_{Al} = 1.8\,\mu\Omega\,cm$, the main conduction channel is localized in the aluminum layer. An estimate of the SQUID resistance in this case is $R_{AL} = \frac{\rho_{Al}l}{2d_{Al}w} \approx 4.5\,\Omega$, which is 5 times smaller than the measured resistance.

Assuming that the aluminum layer is highly resistive $\rho_{Al} = 353\,\mu\Omega\,cm$, most of the current flows through the platinum layer. However, the resistance estimates in this case are $R_{Pt} = \frac{\rho_{Pt}l}{2d_{Pt}w} \approx 75\,\Omega$, which is three times larger than the experimental value.

A possible explanation is the inhomogeneous distribution of low and high-resistivity aluminum in the structure. Low resistivity aluminum has a large coherence length $\xi_{Al} \approx 120$ nm, so this fraction is completely suppressed by the proximity effect with the normal metal. In turn, the coherence length of high resistivity aluminum is a few nanometers, which reduces the influence of the proximity effect, resulting in this fraction becoming a source of superconductivity, providing a high level of kinetic inductance shown in Figure 4b. Normal transport, on the other hand, flows through a heterogeneous composition of low- and high-resistivity aluminum fractions, which explains the intermediate value of the structure's effective resistivity of the order of 4–5 μΩ cm.

5. Conclusion

In conclusion, we have demonstrated the high kinetic inductance of SQUIDs fabricated on an Al/Pt bilayer system across a wide temperature range. The unconventional temperature dependence of the kinetic inductance, $L_K(T)$, is attributed to the formation of a high-resistivity aluminum layer and the proximity effect between aluminum and platinum layers. We developed a microscopic model of electron transport in superconductor-normal metal (SN) bilayers to elucidate this phenomenon, incorporating the proximity effect.

Notably, the Al/Pt bilayer exhibits efficient thermalization, as evidenced by the absence of hysteresis in the current-voltage characteristics. Combined with the high kinetic inductance and robust superconducting behavior, this property positions the Al/Pt system as a promising candidate for advanced superconducting electronic applications.

Conflict of Interest

The authors declare no conflict of interest.

Author Contributions

Ivan A. Nazhestkin: data curation (equal); formal analysis (equal); writing—original draft (equal). **Sergey V. Bakurskiy**: conceptualization (equal); data curation (equal); formal analysis (equal); writing—original draft (equal); writing—review & editing (equal). **Alex A. Neilo**: data curation (equal); formal analysis (equal); writing—original draft (equal). **Irina E. Tarasova**: data curation (equal); formal analysis (equal). **Nidzhat G. Ismailov**: data curation (equal); formal analysis (equal). **Vladimir L. Gurtovoi**: data curation (supporting); formal analysis (supporting). **Sergey V. Egorov**: data curation (equal); formal analysis (equal). **Sergey A. Lisitsyn**: data curation (equal); formal analysis (equal). **Vasily S. Stolyarov**: data curation (equal); formal analysis (equal). **Vladimir N. Antonov**: data curation (equal); formal analysis (equal); supervision (equal). **Valery V. Ryazanov**: data curation (equal); formal analysis (equal); supervision (equal). **Mikhail Y. Kupriyanov**: data curation (equal); formal analysis (equal); supervision (equal); writing—original draft (equal). **Igor I. Soloviev**: data curation (equal); formal analysis (equal); supervision (equal). **Nikolay V. Klenov**: conceptualization (equal); data curation (equal); formal analysis (equal); supervision (equal); writing—original draft (equal); writing—review & editing (equal). **Dmitry S. Yakovlev**: conceptualization (equal); data curation (equal); formal analysis (equal); project administration (lead); supervision (equal); writing—original draft (equal); writing—review & editing (equal).

Data Availability Statement

The data that support the findings of this study are available from the corresponding author upon reasonable request.

[1] P. Krantz, M. Kjaergaard, F. Yan, T. P. Orlando, S. Gustavsson, W. D. Oliver, *Appl. Phys. Rev.* **2019**, *6*, 021318.

[2] J. Clarke, F. K. Wilhelm, *Nature* **2008**, *453*, 1031.

[3] L. Grünhaupt, M. Spiecker, D. Gusenkova, N. Maleeva, S. T. Skacel, I. Takmakov, F. Valenti, P. Winkel, H. Rotzinger, W. Wernsdorfer, A. V. Ustinov, I. M. Pop, *Nat. Mater.* **2019**, *18*, 816.

[4] Z.-L. Xiang, S. Ashhab, J. Q. You, F. Nori, *Rev Mod. Phys.* **2013**, *85*, 623.

[5] N. P. De Leon, K. M. Itoh, D. Kim, K. K. Mehta, T. E. Northup, H. Paik, B. S. Palmer, N. Samarth, S. Sangtawesin, D. W. Steuerman, *Science* **2021**, *372*, eabb2823.

[6] C. E. Murray, *Mater. Sci. Eng.: R: Rep.* **2021**, *146*, 100646.

[7] R. McDermott, *IEEE Trans. Appl. Supercond.* **2009**, *19*, 2.

[8] N. S. Smirnov, E. A. Krivko, A. A. Solovyova, A. I. Ivanov, I. A. Rodionov, *Sci. Rep.* **2024**, *14*, 7326.

[9] A. A. Murthy, P. Masih Das, S. M. Ribet, C. Kopas, J. Lee, M. J. Reagor, L. Zhou, M. J. Kramer, M. C. Hersam, M. Checchin, A. Grassellino, R. Reis, V. P. Dravid, A. Romanenko, *ACS Nano* **2022**, *16*, 17257.

[10] D. Bafia, A. Grassellino, A. Romanenko, *Phys. Rev. Appl.* **2024**, *22*, 024035.

[11] M. Bal, A. A. Murthy, S. Zhu, F. Crisa, X. You, Z. Huang, T. Roy, J. Lee, D. Zanten, R. Pilipenko, I. Nekrashevich, A. Lunin, D. Bafia, Y. Krasnikova, C. J. Kopas, E. O. Lachman, D. Miller, J. Y. Mutus, M. J. Reagor, H. Cansizoglu, J. Marshall, D. P. Pappas, K. Vu, K. Yadavalli, J.-S. Oh, L. Zhou, M. J. Kramer, F. Lecocq, D. P. Goronzy, C. G. Torres-Castanedo, P. G. Pritchard, V. P. Dravid, J. M. Rondinelli, M. J. Bedzyk, M. C. Hersam, J. Zasadzinski, J. Koch, J. A. Sauls, A. Romanenko, A. Grassellino, *npj Quantum Inf.* **2024**, *10*, 43.

[12] J. Burnett, L. Faoro, T. Lindström, *Supercond. Sci. Technol.* **2016**, *29*, 044008.

[13] H. Li, C. Peng, G. Zheng, S. Zhao, Z. Guo, *Phys. Status Solidi RRL* **2023**, *18*, 2300123.

[14] B. A. Mazin, *Microwave Kinetic Inductance Detectors*, California Institute of Technology, Pasadena, CA **2005**.

[15] P. K. Day, H. G. Leduc, A. Goldin, T. Vayonakis, B. A. Mazin, S. Kumar, J. Gao, J. Zmuidzinas, *Nucl. Instrum. Methods Phys. Res.* **2006**, *559*, 561.

[16] W. Guo, X. Liu, Y. Wang, Q. Wei, L. F. Wei, J. Hubmayr, J. Fowler, J. Ullom, L. Vale, M. R. Vissers, J. Gao, *Appl. Phys. Lett.* **2017**, *110*.

[17] A. Roitman, A. Shaulov, Y. Yeshurun, *Supercond. Sci. Technol.* **2023**, *36*, 015002.

[18] A. V. Semenov, I. A. Devyatov, M. P. Westig, T. M. Klapwijk, *Phys. Rev. Appl.* **2020**, *13*, 024079.

[19] G. N. Gol'Tsman, O. Okunev, G. Chulkova, A. Lipatov, A. Semenov, K. Smirnov, B. Voronov, A. Dzardanov, C. Williams, R. Sobolewski, *Appl. Phys. Lett.* **2001**, *79*, 705.

[20] C. M. Natarajan, M. G. Tanner, R. H. Hadfield, *Supercond. Sci. Technol.* **2012**, *25*, 063001.

[21] A. J. Kerman, E. A. Dauler, W. E. Keicher, J. K. W. Yang, K. K. Berggren, G. Gol'Tsman, B. Voronov, *Appl. Phys. Lett.* **2006**, *88*.

[22] C. E. Marvinney, B. E. Lerner, A. A. Puretzky, A. J. Miller, B. J. Lawrie, *Supercond. Sci. Technol.* **2021**, *34*, 035020.

[23] I. Charaev, D. A. Bandurin, A. T. Bollinger, I. Y. Phinney, I. Drozdov, M. Colangelo, B. A. Butters, T. Taniguchi, K. Watanabe, X. He, O. Medeiros, I. Božović, P. Jarillo-Herrero, K. K. Berggren, *Nat. Nanotechnol.* **2023**, *18*, 343.

[24] P. Amari, S. Kozlov, E. Recoba-Pawlowski, Z. Velluire-Pellat, A. Jouan, F. Couëdo, C. Ulysse, J. Briatico, D. Roditchev, N. Bergeal, J. Lesueur, C. Feuillet-Palma, *Phys. Rev. Appl.* **2023**, *20*, 044025.

[25] L. S. Kuzmin, *IEEE Trans. Terahertz Sci. Technol.* **2014**, *4*, 314.

[26] A. S. Mukhin, L. S. Kuzmin, A. V. Chiginev, A. V. Blagodatkin, V. O. Zbrozhek, A. V. Gordeeva, A. L. Pankratov, *AIP Adv.* **2019**, *9*.

[27] A. V. Bogatskaya, N. V. Klenov, A. M. Popov, A. E. Schegolev, P. A. Titovets, M. V. Tereshonok, D. S. Yakovlev, *Nanomaterials* **2024**, *14*, 141.

[28] A. Kozorezov, A. A. Golubov, D. D. E. Martin, P. A. J. De Korte, M. A. Lindeman, R. A. Hijmering, J. Van Der Kuur, H. F. C. Hoevers, L. Gottardi, M. Y. Kupriyanov, J. K. Wigmore, *Appl. Phys. Lett.* **2011**, *99*, 063503.

[29] G. R. Berdiyorov, M. V. Milošević, F. M. Peeters, *Phys. Rev. B: Condens. Matter Mater. Phys.* **2010**, *81*, 144511.

[30] G. P. Papari, V. M. Fomin, *Phys. Status Solidi RRL* **2023**, *17*, 2300038.

[31] S. Kozlov, J. Lesueur, D. Roditchev, C. Feuillet-Palma, *Commun. Phys.* **2024**, *7*, 183.

[32] R. A. Hovhannisyan, T. Golod, V. M. Krasnov, *Phys. Rev. Lett.* **2024**, *132*, 227001.

[33] T. Yamamoto, K. Inomata, M. Watanabe, K. Matsuba, T. Miyazaki, W. D. Oliver, Y. Nakamura, J. S. Tsai, *Appl. Phys. Lett.* **2008**, *93*.

[34] N. Zobrist, B. H. Eom, P. Day, B. A. Mazin, S. R. Meeker, B. Bumble, H. G. LeDuc, G. Coiffard, P. Szypryt, N. Fruitwala, I. Lipartito, C. Bockstiegel, *Appl. Phys. Lett.* **2019**, *115*.

[35] L. J. Splitthoff, J. J. Wesdorp, M. Pita-Vidal, A. Bargerbos, Y. Liu, C. K. Andersen, *Phys. Rev. Appl.* **2024**, *21*, 014052.

[36] M. Malnou, J. Aumentado, M. R. Vissers, J. D. Wheeler, J. Hubmayr, J. N. Ullom, J. Gao, *Phys. Rev. Appl.* **2022**, *17*, 044009.

[37] W. Vine, M. Savytskyi, A. Vaartjes, A. Kringhøj, D. Parker, J. Slack-Smith, T. Schenkel, K. Mølmer, J. C. Mccallum, B. C. Johnson, A. Morello, J. J. Pla, *Sci. Adv.* **2023**, *9*, eadg1593.

[38] B. Ho Eom, P. K. Day, H. G. Leduc, J. Zmuidzinas, *Nat. Phys.* **2012**, *8*, 623.

[39] D. E. Kirichenko, S. Sarwana, A. F. Kirichenko, *IEEE Trans. Appl. Supercond.* **2011**, *21*, 776.

[40] V. Michal, J. Bouat, J.-C. Villégier, J. Sedlacek, in *2009 19th Int. Conf. Radioelektronika*, IEEE, USA **2009**, pp. 161–164.

[41] S. S. Ustavschikov, M. Y. Levichev, I. Y. Pashenkin, A. M. Klushin, D. Y. Vodolazov, *Supercond. Sci. Technol.* **2020**, *34*, 015004.

[42] T. Wolf, N. Bergeal, J. Lesueur, C. J. Fourie, G. Faini, C. Ulysse, P. Febvre, *IEEE Trans. Appl. Supercond.* **2013**, *23*, 1101205.

[43] I. I. Soloviev, V. I. Ruzhickiy, S. V. Bakurskiy, N. V. Klenov, M. Y. Kupriyanov, A. A. Golubov, O. V. Skryabina, V. S. Stolyarov, *Phys. Rev. Appl.* **2021**, *16*, 014052.

[44] A. E. Schegolev, N. V. Klenov, S. V. Bakurskiy, I. I. Soloviev, M. Y. Kupriyanov, M. V. Tereshonok, A. S. Sidorenko, *Beilstein J. Nanotechnol.* **2022**, *13*, 444.

[45] I. Siddiqi, *Nat. Rev. Mater.* **2021**, *6*, 875.

[46] A. Glezer Moshe, E. Farber, G. Deutscher, *Appl. Phys. Lett.* **2020**, *117*.

[47] Y. Schön, J. N. Voss, M. Wildermuth, A. Schneider, S. T. Skacel, M. P. Weides, J. H. Cole, H. Rotzinger, A. V. Ustinov, *npj Quantum Mater.* **2020**, *5*, 18.

[48] I. N. Moskalenko, I. S. Besedin, I. A. Simakov, A. V. Ustinov, *Appl. Phys. Lett.* **2021**, *119*.

[49] R. V. Zakharov, O. V. Tikhonova, N. V. Klenov, I. I. Soloviev, V. N. Antonov, D. S. Yakovlev, *Adv. Quantum Technol.* **2024**, *7*, 2400141.

[50] Z. Velluire-Pellat, E. Maréchal, N. Moulonguet, G. Saïz, G. C. Ménard, S. Kozlov, F. Couëdo, P. Amari, C. Medous, J. Paris, R. Hostein, J. Lesueur, C. Feuillet-Palma, N. Bergeal, *Sci. Rep.* **2023**, *13*, 14366.

[51] F. Friedrich, P. Winkel, K. Borisov, H. Seeger, C. Sürgers, I. M. Pop, W. Wernsdorfer, *Supercond. Sci. Technol.* **2019**, *32*, 125008.

[52] A. Finkler, Y. Segev, Y. Myasoedov, M. L. Rappaport, L. Ne'Eman, D. Vasyukov, E. Zeldov, M. E. Huber, J. Martin, A. Yacoby, *Nano Lett.* **2010**, *10*, 1046.

[53] S. Avraham, S. Bachar, A. Glezer Moshe, E. Farber, G. Deutscher, *Appl. Phys. Lett.* **2023**, *123*.

[54] H. Dausy, L. Nulens, B. Raes, M. J. Van Bael, J. Van De Vondel, *Phys. Rev. Appl.* **2021**, *16*, 024013.

[55] D. Niepce, J. Burnett, J. Bylander, *Phys. Rev. Appl.* **2019**, *11*, 044014.

[56] J. T. Peltonen, P. C. J. J. Coumou, Z. H. Peng, T. M. Klapwijk, J. S. Tsai, O. V. Astafiev, *Sci. Rep.* **2018**, *8*, 10033.

[57] A. G. Shishkin, O. V. Skryabina, V. L. Gurtovoi, S. E. Dizhur, M. I. Faley, A. A. Golubov, V. S. Stolyarov, *Supercond. Sci. Technol.* **2020**, *33*, 065005.

[58] Z. Sofer, A. Shaulov, Y. Yeshurun, *Sci. Rep.* **2022**, *12*, 22027.

[59] J. Zotova, A. Semenov, R. Wang, Y. Zhou, O. Astafiev, J.-S. Tsai, *Phys. Rev. Appl.* **2024**, *21*, 024059.

[60] D. S. Yakovlev, I. A. Nazhestkin, N. G. Ismailov, S. V. Egorov, V. N. Antonov, V. L. Gurtovoi, *Symmetry* **2023**, *15*, 550.

[61] D. Lopez-Nunez, Q. P. Montserrat, G. Rius, E. Bertoldo, A. Torras-Coloma, M. Martínez, P. Forn-Díaz (Preprint), arXiv:2311.14119, v1, Submitted: Nov. **2023**.

[62] V. S. Stolyarov, D. Roditchev, V. L. Gurtovoi, S. N. Kozlov, D. S. Yakovlev, O. V. Skryabina, V. M. Vinokur, A. A. Golubov, *Adv. Quantum Technol.* **2022**, *5*, 2100124.

[63] D. S. Yakovlev, A. V. Frolov, I. A. Nazhestkin, A. G. Temiryazev, A. P. Orlov, J. Shvartzberg, S. E. Dizhur, V. L. Gurtovoi, R. Hovhannisyan, V. S. Stolyarov, *Adv. Phys. Res.* **2024**, *3*, 2400108.

[64] P. De Gennes, *Superconductivity of Metals and Alloys*, W. A. Benjamin Inc, New York, NY **1966**.

[65] A. Golubov, M. Kupriyanov, V. Lukichev, A. Orlikovskii, *Mikroelektronika* **1983**, *12*, 355.

[66] M. M. Khapaev, M. Y. Kupriyanov, E. Goldobin, M. Siegel, *Supercond. Sci. Technol.* **2003**, *16*, 24.

[67] C. D. Tesche, J. Clarke, *J. Low Temp. Phys.* **1977**, *29*, 301.

[68] I. I. Soloviev, N. V. Klenov, A. E. Schegolev, S. V. Bakurskiy, M. Y. Kupriyanov, *Supercond. Sci. Technol.* **2016**, *29*, 094005.

[69] K. D. Usadel, *Phys. Rev. Lett.* **1970**, *25*, 507.

[70] M. Y. Kuprianov, V. F. Lukichev, *Zh. Eksp. Teor. Fiz.* **1988**, *94*, 139.

[71] A. Golubov, *Superconducting Superlattices and Multilayers*, Vol. *2157*, SPIE, Los Angeles, CA **1994**, pp. 353–362.

[72] A. A. Golubov, M. Y. Kupriyanov, *Phys. C* **1996**, *259*, 27.

[73] W. Belzig, C. Bruder, G. Schön, *Phys. Rev. B* **1996**, *54*, 9443.

[74] Y. V. Fominov, M. V. Feigel'Man, *Phys. Rev. B* **2001**, *63*, 094518.

[75] A. A. Mazanik, Y. Fominov, *Ann. Phys.* **2023**, *449*, 169199.

[76] V. S. Stolyarov, T. Cren, C. Brun, I. A. Golovchanskiy, O. V. Skryabina, D. I. Kasatonov, M. M. Khapaev, M. Y. Kupriyanov, A. A. Golubov, D. Roditchev, *Nat. Commun.* **2018**, *9*, 2277.

[77] A. Dominjon, M. Sekine, K. Karatsu, T. Noguchi, Y. Sekimoto, S. Shu, S. Sekiguchi, T. Nitta, *IEEE Trans. Appl. Supercond.* **2016**, *26*, 2400206.

[78] D. Y. Vodolazov, *JETP Lett.* **2023**, *118*, 773.

[79] P. Marychev, D. Y. Vodolazov, *J. Phys.: Condens. Matter* **2021**, *33*, 385301.

[80] T. E. Golikova, F. Hübler, D. Beckmann, N. V. Klenov, S. V. Bakurskiy, M. Y. Kupriyanov, I. E. Batov, V. V. Ryazanov, *JETP Lett.* **2013**, *96*, 668.

[81] M. Flokstra, R. Stewart, C.-M. Yim, C. Trainer, P. Wahl, D. Miller, N. Satchell, G. Burnell, H. Luetkens, T. Prokscha, A. Suter, E. Morenzoni, I. V. Bobkova, A. M. Bobkov, S. Lee, *Nat. Commun.* **2023**, *14*, 5081.

[82] A. Catalano, J. Goupy, H. Le Sueur, A. Benoit, O. Bourrion, M. Calvo, A. D'Addabbo, L. Dumoulin, F. Levy-Bertrand, J. Macías-Pérez, S. Marnieros, N. Ponthieu, A. Monfardini, *Astron. Astrophys.* **2015**, *580*, A15.

[83] J. Hu, M. Salatino, A. Traini, C. Chaumont, F. Boussaha, C. Goupil, M. Piat, *J. Low Temp. Phys.* **2020**, *199*, 355.

[84] G. Wang, P. S. Barry, T. Cecil, C. L. Chang, J. Li, M. Lisovenko, V. Novosad, Z. Pan, V. G. Yefremenko, J. Zhang, *IEEE Trans. Appl. Supercond.* **2023**, *33*, 2400306.

[85] L. N. Cooper, *Phys. Rev. Lett.* **1961**, *6*, 689.

[86] W. L. Mcmillan, *Phys. Rev.* **1968**, *175*, 537.

[87] M. M. Khapaev, A. Y. Kidiyarova-Shevchenko, P. Magnelind, M. Y. Kupriyanov, *IEEE Trans. Appl. Supercond.* **2001**, *11*, 1090.

[88] L. Meti, G. Long, T. Godfrey, J. Potter, D. Cox, G. Chapman, J. Gallop, E. Romans, L. Hao, *IEEE Trans. Appl. Supercond.* **2023**, *33*, 3244771.

[89] T. Godfrey, G. Long, J. Gallop, D. Cox, E. Polychroniou, J. Chen, E. Romans, L. Hao, *IEEE Trans. Appl. Supercond.* **2020**, *30*, 2998374.

[90] R. R. Altunin, E. T. Moiseenko, S. M. Zharkov, *Phys. Solid State* **2018**, *60*, 1413.

[91] F. Levy-Bertrand, T. Klein, T. Grenet, O. Dupré, A. Benoît, A. Bideaud, O. Bourrion, M. Calvo, A. Catalano, A. Gomez, J. Goupy, L. Grünhaupt, U. Luepke, N. Maleeva, F. Valenti, I. M. Pop, A. Monfardini, *Phys. Rev. B* **2019**, *99*, 094506.

[92] N. Maleeva, L. Grünhaupt, T. Klein, F. Levy-Bertrand, O. Dupre, M. Calvo, F. Valenti, P. Winkel, F. Friedrich, W. Wernsdorfer, A. V. Ustinov, H. Rotzinger, A. Monfardini, M. V. Fistul, I. M. Pop, *Nat. Commun.* **2018**, *9*, 3889.

[93] T. E. Wilson, *Meas. Sci. Technol.* **2007**, *18*, N53.

[94] L. Grünhaupt, N. Maleeva, S. T. Skacel, M. Calvo, F. Levy-Bertrand, A. V. Ustinov, H. Rotzinger, A. Monfardini, G. Catelani, I. M. Pop, *Phys. Rev. Lett.* **2018**, *121*, 117001.

[95] P. Kamenov, W.-S. Lu, K. Kalashnikov, T. Dinapoli, M. T. Bell, M. E. Gershenson, *Phys. Rev. Appl.* **2020**, *13*, 054051.